Published in final edited form as:
Nat Nanotechnol. 2008 February ; 3(2): 88–92. doi:10.1038/nnano.2008.26.

Bottom-up assembly of large-area nanowire resonator arrays

MINGWEI LI[1,†], **RUSTOM B. BHILADVALA**[1,2,†,*], **THOMAS J. MORROW**[3], **JAMES A. SIOSS**[3], **KOK-KEONG LEW**[4,‡], **JOAN M. REDWING**[4], **CHRISTINE D. KEATING**[3], and **THERESA S. MAYER**[1,2,*]

1 *Department of Electrical Engineering, The Pennsylvania State University, University Park, Pennsylvania 16802, USA*

2 *Materials Research Institute, The Pennsylvania State University, University Park, Pennsylvania 16802, USA*

3 *Department of Chemistry, The Pennsylvania State University, University Park, Pennsylvania 16802, USA*

4 *Department of Materials Science and Engineering, The Pennsylvania State University, University Park, Pennsylvania 16802, USA*

Abstract

Directed-assembly of nanowire-based devices[1] will enable the development of integrated circuits with new functions that extend well beyond mainstream digital logic. For example, nanoelectromechanical resonators are very attractive for chip-based sensor arrays[2] because of their potential for ultrasensitive mass detection[3–6]. In this letter, we introduce a new bottom-up assembly method to fabricate large-area nanoelectromechanical arrays each having over 2,000 single-nanowire resonators. The nanowires are synthesized and chemically functionalized before they are integrated onto a silicon chip at predetermined locations. Peptide nucleic acid probe molecules attached to the nanowires before assembly maintain their binding selectivity and recognize complementary oligonucleotide targets once the resonator array is assembled. The two types of cantilevered resonators we integrated here using silicon and rhodium nanowires had Q-factors of ~4,500 and ~1,150, respectively, in vacuum. Taken together, these results show that bottom-up nanowire assembly can offer a practical alternative to top-down fabrication for sensitive chip-based detection.

Our hybrid nanoelectromechanical systems (NEMS) array integration strategy combines deterministic bottom-up nanowire (NW) assembly with conventional top-down microfabrication as illustrated in Fig. 1. Here we show the flexibility of this approach by fabricating resonators using two types of NWs—semiconducting silicon (Si) or metallic rhodium (Rh)—synthesized off-chip with different growth methods. The SiNWs grown by the Au-catalysed vapour–liquid–solid (VLS) technique are predominately single-crystal and oriented in the $\langle 111 \rangle$ or $\langle 112 \rangle$ growth directions[7]. In contrast, RhNWs electrodeposited within the pores of anodic aluminium oxide membranes are polycrystalline, with an average grain size of 5 nm (ref. 8). This assembly method is quite general and can be extended to many other NW materials[1,9] (for example, multisegment metal, magnetic, oxide or piezoelectric materials) and geometries[10] (for example, hollow tube or flat belt).

Correspondence and requests for materials should be addressed to R.B.B. and T.S.M.

[†] These authors contributed equally to this work.

[‡] Present address: Power Electronics Branch, Naval Research Laboratory, Washington DC 22375, USA

[*] e-mail: rbb16@psu.edu; tsm2@psu.edu

Bottom-up assembly is used to position single NWs at lithographically defined locations on a Si chip for fabricating multiplexed arrays. Unlike earlier reports of NW assembly[11–15], three separate mechanisms are combined to achieve high-yield NW integration over centimetre-scale chip areas: electric-field forces, capillary forces and NW lift-off. As illustrated in Fig. 1, we patterned arrays of wells in a sacrificial insulating photoresist layer covering metal guiding electrodes defined on the chip surface. An alternating voltage in the kilohertz range was applied between the guiding electrodes to produce spatially confined electric fields that polarize NWs in suspension[11]. Long-range dielectrophoretic forces attract the NWs to the surface and align them along the electric-field gradient. Single NWs are further centred in the electrode gaps by short-range capacitive forces between the NWs and guiding electrodes. The NWs that are preferentially aligned in the wells are retained there by capillary forces produced during evaporation of the suspending liquid within each well (Fig. 1b; see also Supplementary Information, Fig. S1)[16].

We completed our NEMS resonator integration by electrodepositing a thick metal clamp at one end of the NW aligned in each well and dissolving the photoresist layers. This was accomplished by patterning a window to define the metal clamp in a second photoresist masking layer. The pattern was transferred into the sacrificial photoresist to expose the NW tips and the unmasked regions of the guiding electrodes (Fig. 1c). Au metal was electrodeposited in the open windows until it completely surrounded the NW tips and reached the top surface of the second photoresist layer. The photoresist was dissolved to lift off any misaligned NWs and leave parallel arrays of free-standing single-NW cantilevers (Fig. 1d; see also Supplementary Information, Fig. S2) as shown in the field-emission scanning electron microscope (FE-SEM) images of Fig. 2a,b. Typical defects include missing and multiple NWs (aggregates or end-to-end chains), which occur in nearly equal numbers using our laboratory-scale NW synthesis, delivery and assembly procedures. Despite these defects, we observe high yields (~80%) of well-aligned single NWs assembled in arrays containing over 2,000 resonators; even higher device yields are expected by implementing more controlled and optimized nanomanufacturing processes.

Key attributes of this hybrid strategy are shown in the FE-SEM images of Si- and RhNW resonators in Fig. 2c–e. First, the electrodeposited metal fully surrounds each NW to form a clamp with nearly vertical sidewalls that secures the NW to the Si chip. This differs significantly from previous NW- (ref. 17) and nanotube-based NEMS (ref. 18) that use a thin evaporated top metal as a mechanical anchor and are released by selective wet etching of an underlying SiO_2 layer. For such devices, the clamp can be expected to lower the Q-factor and mechanical stiffness, as in top-down NEMS (ref. 19). Second, the cantilevered NWs are straight and parallel to the chip surface, including RhNWs (Fig. 2e). Thus, the deformation observed in NEMS fabricated using sputtered or evaporated metal thin films[20] due to stress evolution during the cantilever release process is eliminated using metal NWs synthesized off-chip. Third, the metal clamp provides a direct electrical connection between the chip and conductive NWs, which can be used for multiplexed electrical drive and detection of single NWs in the array.

Importantly, the NWassembly and subsequent fabrication steps eliminate the need for the chemical etchants used in cantilever release processes, making the present process compatible with the chemically functionalized NWs used in biosensor arrays. In contrast to top-down fabricated biosensors, our approach allows the attachment of molecules to the NW surfaces under optimized conditions off-chip, followed by assembly of the NWs into arrays on the chip (Fig. 1a,e). As a proof of principle, we covalently attached peptide nucleic acid (PNA) probe molecules designed to selectively detect oligonucleotide sequences found in the genomes of hepatitis C (HCV) or hepatitis B (HBV) viruses to different batches of SiO_2-coated RhNWs before on-chip integration[21]. Figure 2f,g (right panels) shows fluorescence optical microscope images of these NW resonators after exposure to fluorescently labelled oligonucleotides complementary to the HCV probes. The strong fluorescence signal observed for the complementary probes and the very little fluorescence for the non-complementary probes indicate that the probe PNA maintains its binding selectivity throughout the process. PNA probe molecules can be applied to mass-based nucleic acid detection using NW resonators such as those described here, or for alternative biosensing strategies based on conductance changes of NW field-effect transistors[22].

Resonator performance was investigated by measuring the resonant oscillations of Si- and RhNW cantilevers at high vacuum (5×10^{-10} atm). Cantilevered rather than doubly clamped NW resonators were used to eliminate uncertainty in the measured elastic properties from beam-tension effects[23]. The NWs were harmonically forced using either piezo or electrical drive methods (see Supplementary Information, Figs S3–S5), and their motion was sensed using laser interferometry[24]. Figure 3a shows that the resonance spectra for Si- and RhNWs fit well to a lorentzian function, and that forward and reverse frequency sweeps are coincident. Additionally, the resonant peak frequency is constant over a decade of driving voltage, and the peak amplitude varies linearly with drive voltage (Fig. 3b), confirming that the resonators operate in the linear regime. The Q-factors determined for the Si- and RhNW resonators are 4,500 ± 500 and 1,150 ± 150 (averaged over many NW resonators), respectively. The linear response and high Q values make resonators such as these strong candidates for sensitive resonance-based detection schemes[6].

We evaluated NW resonator properties using the expression for the resonance frequency f of a linear, cylindrical flexural cantilever beam with $Q \gg 1$,

$$f=\left[\frac{1}{8\pi}\left(\frac{\beta^4 E}{\rho}\right)^{\frac{1}{2}}\right]\frac{D}{L^2}, \qquad (1)$$

where E and ρ are Young’s modulus and density of the NW material respectively, and D and L are the NW diameter and length. The constant β is equal to 1.88 for a rigidly clamped cantilever vibrating in the fundamental mode[25]. Values of f measured for 16 SiNW cantilevers with different geometric ratios D/L^2 are plotted in Fig. 3c and agree well with equation (1). The very small scatter in measured f also shows that NEMS fabricated using our hybrid integration strategy are very uniform. Specifically, the factor $(\beta^4 E)^{1/2}$ is nearly constant, demonstrating that device-to-device variations in the clamp boundary condition (β) and NW Young’s modulus are negligible (assuming constant ρ, and noting that the $\langle 111\rangle$ and $\langle 112\rangle$ directions of Si have nearly identical elastic constants[26]). This reproducibility in clamping can be difficult to achieve for thin-film resonators released by selective etching, because the ratio of clamp undercut to resonator length varies when devices of different geometries are fabricated on the same chip. Using equation (1), we calculate a SiNW Young’s modulus $E = 152 \pm 6$ GPa (see Supplementary Information, Table S1). This value is similar to the $E \approx 158$ GPa measured by static deflection of suspended SiNW beams using atomic force microscopy[27]. A study of Young’s moduli for different metal NW resonators is reported elsewhere[28].

As air damping can strongly affect the Q-factor, we measured resonance spectra of Si- and RhNWs at pressures from high vacuum (5×10^{-10} atm) to 1 atm (Fig. 4a,b). The high-vacuum values of Q are maintained well into the medium vacuum range (up to pressures of 10^{-4} and 10^{-2} atm for the Si- and RhNWs, respectively). Interestingly, when air damping begins to dominate at higher pressures, the Q-factor curves for these two resonators cross, with $Q_{\mathrm{RhNW}} \approx 14 \times Q_{\mathrm{SiNW}}$ at 1 atm. The change in Q-factor due to gas damping is given by[29]

$$Q=\frac{2\pi fm}{C_s+C_f}=Q_s\left(1+\frac{C_f}{C_s}\right)^{-1} \tag{2}$$

where m is the mass of the NW, C_s is the pressure-independent solid damping coefficient from all sources other than the gas and C_f is the pressure-dependent fluid damping coefficient. Equations (1) and (2) show that $2\pi fm$ depends on resonator geometry and material properties; this factor is seven times larger for the RhNW than for the SiNW resonator measured here. At the high-vacuum limit where $C_f \approx 0$, the ratio of measured Q-values is $Q_{s,RhNW}/Q_{s,SiNW} \approx 0.24$, indicating that $C_{s,RhNW} \approx 30 \times C_{s,SiNW}$. At atmospheric pressure where $C_f \gg C_s$, the Q-factors are determined only by $2\pi fm$ and C_f. Simple scaling ($C_f \approx DL$) assuming free molecular flow yields $Q_{RhNW}/Q_{SiNW} \approx 17$ at 1 atm, confirming the experimentally observed curve crossing for these NW resonators. Earlier experimental work[30] suggests that measured Q-factors should deviate from the free-molecular solution (Fig. 4b, dashed line) at a Knudsen number Kn = 10 and begin a transition towards continuum flow; higher Q-factor values than obtained from this solution are expected[29] for Kn < 10. Our resonators have Q-factors that deviate at a higher pressure, corresponding to Kn ≈ 0.5 (based on resonator width). Recent experiments with other thin-film NEMS resonators[3] show that the deviation occurs at Kn values between 0.1 and 0.8, which is similar to the data presented here. The source of this difference is not well understood, and is the subject of continued investigation. These data and analysis underscore the importance of accounting for both geometric and material properties when designing NEMS resonators for sensitive resonance-based detection in air.

In conclusion, we have demonstrated a bottom-up assembly method for integrating NWs synthesized and chemically functionalized off-chip into arrays of NEMS resonators on a Si chip. Three mechanisms were combined to achieve high-yield positioning of over 2,000 single NWs in each array: electric-field forces, capillary forces and NW lift-off. PNA probe molecules attached to NWs prior to assembly bound selectively to complementary oligonucleotide targets following device fabrication. The integrated Si- and RhNW resonators had uniform and reproducible clamps, and operated in the linear regime with vacuum Q-factors of ~4,500 and ~1,150, respectively. The pressure dependence of measured Q-factor values is determined by the NW geometry and material properties. This approach promises to expand the range of NW materials, geometries and surface chemistries that can be integrated on a chip, and to enable multiplexed arrays of individually addressable NW devices.

METHODS

NW SYNTHESIS

Anodic aluminium oxide (AAO) membranes (Anodisc25, Whatman Scientific) were used as templates for NW synthesis. SiNWs were grown by the VLS technique using Au catalyst nanoparticles electrodeposited within the pores of the membrane using previously reported methods[7]. The growth was carried out in a hot-wall furnace using a mixture of SiH_4 in H_2 at 500 °C, with a total pressure of 13 torr and SiH_4 partial pressure of 0.65 torr. The SiNW growth rate was ~1 $\mu m\ min^{-1}$. The portions of the SiNWs that grew outside the membrane were released into isopropyl alcohol (IPA) by sonication. The RhNWs were grown by galvanostatic electrodeposition of Rh from Rhodium S-Less plating solution (Technic) using a Ag working electrode and Pt counter-electrode. The RhNW growth rate at a constant current of 1.65 mAwas 0.8 $\mu m\ h^{-1}$. Ag was removed from the membrane using 7.5 M HNO_3, and the RhNWs released into IPA by dissolving the membrane in 3.0 M NaOH.

NW RESONATOR INTEGRATION

Interdigitated guiding metal electrodes (20-nm Ti/60-nm Au) were patterned on a (100) Si substrate protected by a 1-μm thermally grown SiO_2 layer using a metal lift-off process. The substrate was then coated with 1 μm of deep-ultraviolet (DUV) photoresist (PMGI-SF-11, MicroChem) and arrays of wells were patterned to a depth of 500–700 nm (Fig. 1b). Then, 10 μl of the NW suspension was injected between the substrate and a cover slip that was held 1 mm above the surface by spacers. A 7 V_{rms}, 10 kHz sinusoidal voltage was applied between the guiding electrodes to align the NWs across the electrode gaps. The NWs preferentially assembled into the wells due to the higher field strength in these regions (Fig. 1b; see Supplementary Information, Fig. S1). The metal clamp windows were patterned in a second 1-μm layer of photoresist (Shipley 1811, Shipley), and transferred into the PMGI by DUV flood exposure and removal in developer (PMGI-101, Microchem), leaving the NW tips and underlying metal electrodes exposed. The metal clamps were electrodeposited (TG-25 RTU, Technic) in the windows using the guiding electrode as the working electrode. A deposition rate of ~ 0.1 μm min^{-1} was obtained using a pulsed current of I_{peak} = 1 mA at a duty cycle of 0.6/0.3 ms. The cantilevered NWs were released by dissolving both layers of photoresist (Microposit 1165, MicroChem), rinsing the chip in deionized water followed by ethanol, and drying the chip in a critical point dryer to prevent the NW cantilevers from adhering to the substrate. NWs misaligned outside the wells were also lifted off when the photoresist was dissolved (Fig. 1d; see Supplementary Information, Fig. S2).

COVALENT ATTACHMENT AND HYBRIDIZATION OF PNA

Covalent attachment of PNA to the SiO_2-coated RhNWs was based on previously reported methods[21]. PNA sequences used were 5′-Cys-GAG TAG TGT T-EE-3′ and 5′-Cys-CTC AAT CTC G-EE-3′, where E denotes the solubility enhancer [(2-amino-ethyl)-(2-{[*bis*-(2-methoxy-ethyl)-carbamoyl]-methoxy}-acetyl)-amino]-acetic acid. Here, sulphosuccinimidyl 4-[*N*-maleimidomethyl] cyclohexane-1-carboxylate (sulpho-SMCC) was used to crosslink the amino group on 3-aminopropyltrimethoxy silane (APTMS) to the thiol on the cysteine residue synthesized onto the 5′ end of the PNA sequences (Biosynthesis). PNA attachment was achieved by mixing 100 μl of the silica/sulpho-SMCC coated RhNWs suspended in 300 mM NaCl 10 mM Na phosphate (PBS) with 100 μl of the 20 μM PNA solution for 24 h while vortexing. The NWs were washed three times with PBS then three times with ethanol.

Hybridization of 5′-Alexa Fluor 488-TTC GCG ACC CAA CAC TAC TC-3′ target DNA (Integrated DNA Technologies) was performed after NW assembly and integration by incubation with 0.4 μM of the appropriate DNA in PBS at 25 °C for ~15 h, followed by rinsing in PBS. This sequence is complementary to one of the two probe PNA sequences (5′-Cys-GAG TAG TGT T-EE-3′). Note that although HCV is an RNA virus, we are using a DNA oligonucleotide as a mimic of this portion of the HCV sequence here.

RESONANCE CHARACTERIZATION

The resonant oscillation of cantilevered Si- and RhNWs was driven and measured using a spectrum analyser (Agilent E4402B) equipped with a tracking generator. Chips containing NW cantilever arrays were mounted on a piezoceramic actuator disk (extracted from a Radio Shack 273-059 buzzer). NWs were vibrated either using the piezo disk or by an electrical signal applied between the metal clamp and electrode below the suspended tip. The driving voltage was provided by the tracking generator of the spectrum analyser. The chips were mounted in a vacuum chamber with absolute pressure controlled from 5×10^{-10} atm to 1 atm by pumping out or introducing dry nitrogen. A laser interferometry technique[24] was used to translate the displacement of single-NW resonators into an optical signal, which was monitored using an a.c.-coupled photodetector (New Focus 1601-FS-AC). Resonant amplitude information was extracted from the photodetector signal using the spectrum analyser and averaging over 100 continuous sweeps in 25 s for one spectrum.

Supplementary Material

Refer to Web version on PubMed Central for supplementary material.

Acknowledgements

We acknowledge primary support from the National Institutes of Health (CA118591). Additional support was provided by the National Science Foundation (DMR-0213623, CHE-0304575, CCR-0303976), and Tobacco Settlement funds from the Pennsylvania Department of Health, which specifically disclaims responsibility for any analyses, interpretations, or conclusions. C.D.K. received partial support from the National Institutes of Health (R01 EB00268). The authors also acknowledge use of facilities at the Penn State University site of the National Science Foundation National Nanotechnology Infrastructure Network.

References

1. Lieber CM, Wang ZL. Functional nanowires. MRS Bull 2007;32:99–108.
2. Zheng GF, et al. Multiplexed electrical detection of cancer markers with nanowire sensor arrays. Nature Biotechnol 2005;23:1294–1301. [PubMed: 16170313]
3. Li M, Tang HX, Roukes ML. Ultra-sensitive NEMS-based cantilevers for sensing, scanned probe, and very high-frequency applications. Nature Nanotech 2007;2:114–120.
4. Yang YT, Callegari C, Feng XL, Ekinci KL, Roukes ML. Zeptogram-scale nanomechanical mass sensing. Nano Lett 2006;6:583–586. [PubMed: 16608248]
5. Craighead HG. Nanoelectromechanical systems. Science 2000;290:1532–1535. [PubMed: 11090343]
6. Lavrik NV, Sepaniak MJ, Datskos PG. Cantilever transducers as a platform for chemical and biological sensors. Rev Sci Instrum 2004;75:2229–2253.
7. Wang Y, et al. Use of phosphine as an n-type dopant source for vapor–liquid–solid growth of silicon nanowires. Nano Lett 2005;5:2139–2143. [PubMed: 16277441]
8. Tian M, et al. Electrochemical growth of single-crystal metal nanowires via a two-dimensional nucleation and growth mechanism. Nano Lett 2003;3:919–923.
9. Keating CD, Natan MJ. Striped metal nanowires as building blocks and optical tags. Adv Mater 2003;15:451–454.
10. Xia Y, et al. One-dimensional nanostructures: synthesis, characterization, and applications. Adv Mater 2003;15:353–389.
11. Smith PA, et al. Electric-field assisted assembly and alignment of metallic nanowires. Appl Phys Lett 2000;77:1399–1401.
12. Huang Y, Duan X, Wei Q, Lieber CM. Directed assembly of one-dimensional nanostructures into functional networks. Science 2001;26:630–633. [PubMed: 11158671]
13. Whang D, Jin S, Wu Y, Lieber CM. Large-scale hierarchial organization of nanowire arrays for integrated nanosystems. Nano Lett 2003;3:1255–1259.
14. Huang J, Fan R, Connor S, Yang P. One-step patterning of aligned nanowire arrays by programmed dip coating. Angew Chem Int Edn 2007;46:2414–2417.
15. Liu M, et al. Self-assembled magnetic nanowire arrays. Appl Phys Lett 2007;90:103105.
16. Yin Y, et al. Template-assisted self-assembly: A practical route to complex aggregates of monodispersed colloids with well-defined sized, shapes, and structures. J Am Chem Soc 2001;123:8718–8729. [PubMed: 11535076]
17. Husain A, et al. Nanowire-based very-high-frequency electromechanical resonator. Appl Phys Lett 2003;83:1240–1242.
18. Sazonova V, et al. A tunable carbon nanotube electromechanical oscillator. Nature 2004;431:284–287. [PubMed: 15372026]
19. Davis ZJ, Boisen A. Aluminum nanocantilevers for high sensitivity mass sensors. Appl Phys Lett 2005;87:013102.

20. Fang W, Wickert JA. Determining mean and gradient residual stresses in thin films using micromachined cantilevers. J Micromech Microeng 1996;6:301–309.
21. Sioss JA, Stoermer RL, Sha MY, Keating CD. Silica coated, Au/Ag striped nanowires for bioanalysis. Langmuir 2007;23:11334–11341. [PubMed: 17880120]
22. Cui Y, Wei QQ, Park HK, Lieber CM. Nanowire nanosensors for highly sensitive and selective detection of biological and chemical species. Science 2001;293:1289–1292. [PubMed: 11509722]
23. Sahai TS, Bhiladvala RB, Zehnder AT. Thermomechanical transitions in doubly-clamped micro-oscillators. Int J Nonlinear Mech 2007;42:596–607.
24. Kouh T, Karabacak D, Kim DH, Ekinci KL. Diffraction effects in optical interferometric displacement detection in nanoelectromechanical systems. Appl Phys Lett 2005;86:013106.
25. Blevins, RD. Formulas for Natural Frequency and Mode Shape. Robert E. Krieger Publishing Company; Malabar, FL: 1986.
26. Anastassakis E, Siakavellas M. Elastic properties of textured diamond and silicon. J Appl Phys 2001;90:144–152.
27. Heidelberg A, et al. A generalized description of the elastic properties of nanowires. Nano Lett 2006;6:1101–1106. [PubMed: 16771561]
28. Li M, Mayer TS, Sioss JA, Keating CD, Bhiladvala RB. Template-grown metal nanowires as resonators: performance and characterization of dissipative and elastic properties. Nano Lett 2007;7:3281–3284. [PubMed: 17967041]
29. Bhiladvala RB, Wang Z. J Effect of fluids on the *Q*-factor and resonance frequency of oscillating micrometer and nanometer scale beams. Phys Rev E 2004;69:036307.
30. Schaaf, S.; Chambre, P. Flow of Rarefied Gases. Princeton Univ. Press; Princeton, NJ: 1961.

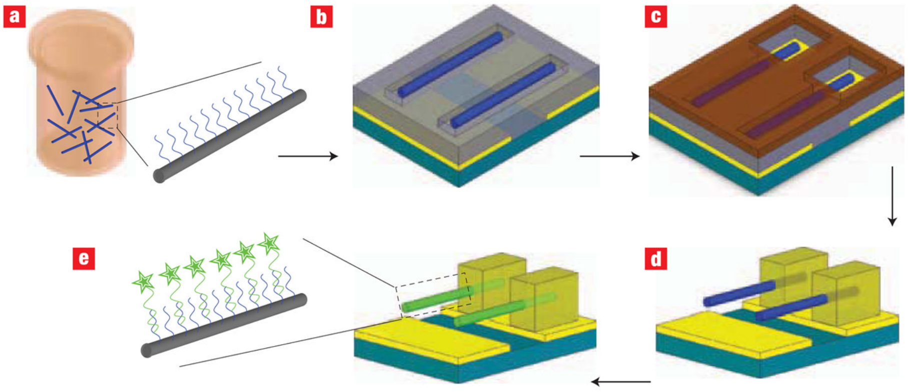

Figure 1. Bottom-up integration scheme used to fabricate NW resonator arrays

a, PNA probe molecules are attached to the NW surface. **b**, Electric-field forces are used to preferentially align single NWs in wells patterned in a sacrificial photoresist layer. The photoresist thickness at the base of the well determines the NW suspended height. **c**, Individual clamp windows are defined in a second photoresist layer. **d**, Metal clamps are electrodeposited around the NW tips. The photoresist is dissolved to suspend the clamped NWs and lift off any that are misaligned (unclamped). **e**, The NWs are exposed to fluorescently labelled complementary and non-complementary targets to confirm detection selectivity. This integration method facilitates future electrical connection of single NWs to underlying Si circuitry.

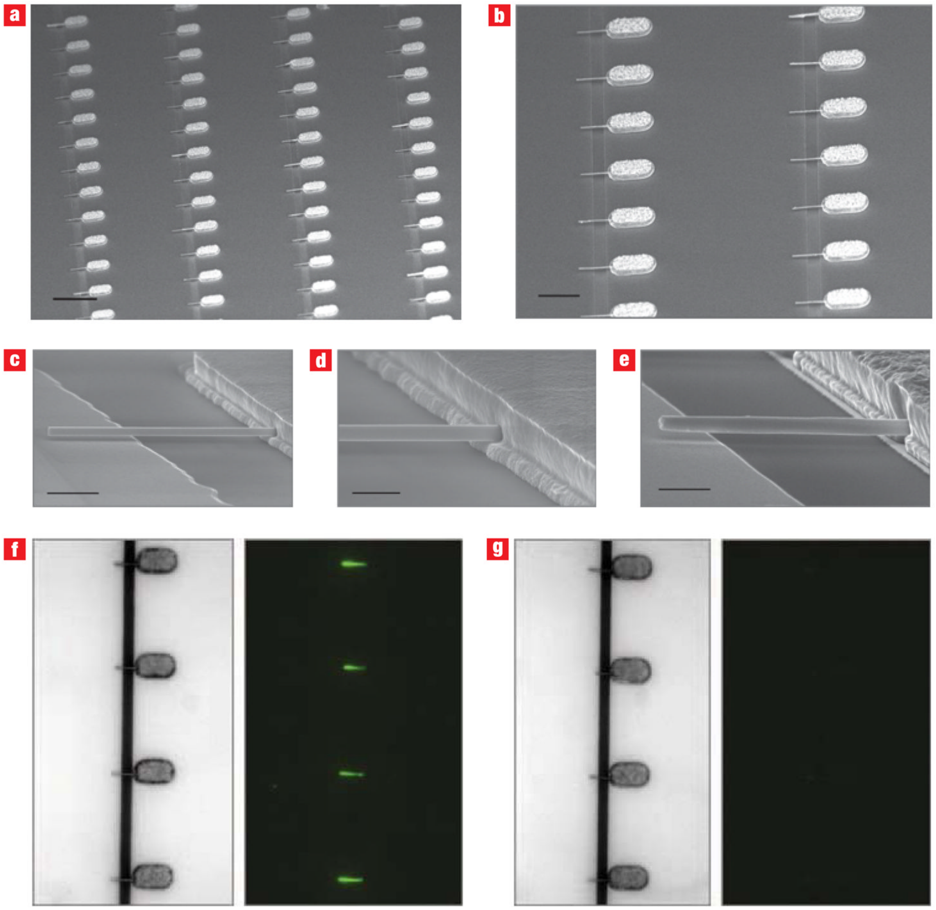

Figure 2. Fabricated Si- and RhNW resonator arrays and selective binding of oligonucleotide targets

a–e, FE-SEM images: RhNW resonator arrays showing a high yield of single NWs positioned at predefined locations on the chip (**a**,**b**); cantilevered SiNW resonator clamped with electrodeposited Au (right), and suspended 300 nm above the Au electrode (left) (**c**,**d**) (these electrodes are used to electrically drive the resonators); cantilevered RhNW resonator (**e**). **f**,**g**, Bright-field (left panels) and fluorescence (right panels) optical microscope images of NWs coated with different PNA probe sequences for HCV (**f**) and HBV (**g**) after exposure to fluorescently labelled oligonucleotides complementary only to the HCV probe. Scale bars in **a–e** are 20, 10, 2, 1 and 1 µm, respectively.

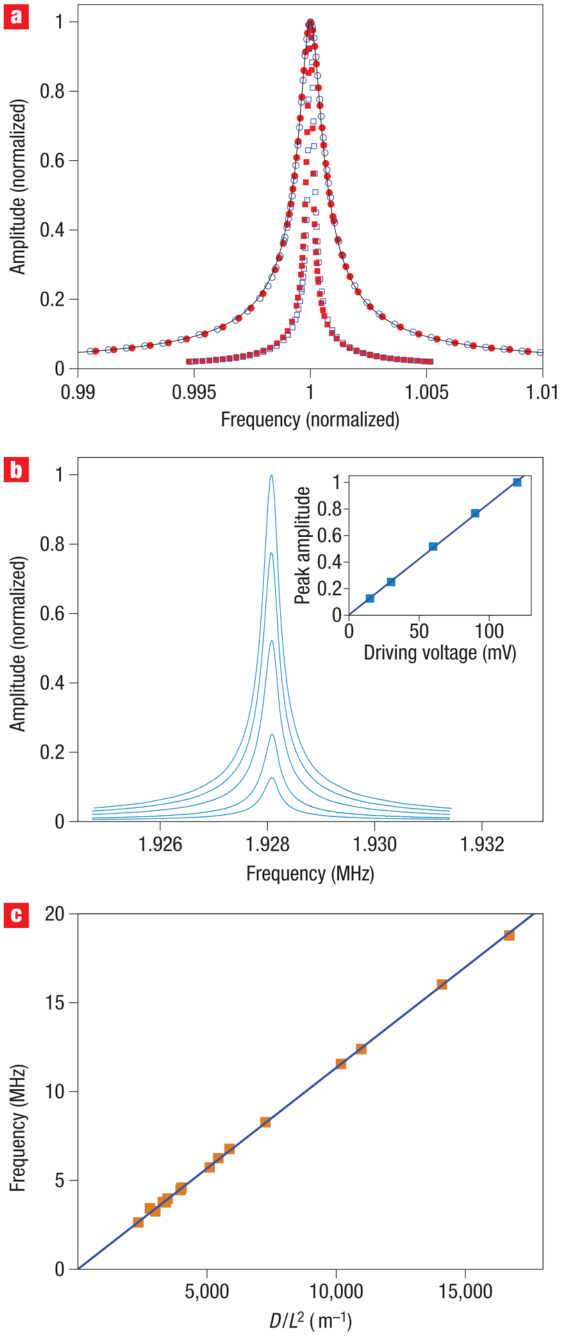

Figure 3. Resonant response at room temperature and high vacuum (5×10^{-10} atm) using an electrical drive method

a, Normalized measured spectra (symbols) and lorentzian fit (line) for Si- (inner curve) and RhNW (outer curve) resonators. Filled and open symbols correspond to increasing and decreasing frequency sweeps, respectively. (Si- and RhNWs: *Q*-factors are 4,830 and 1,080; resonance frequencies are 1.928 and 7.186 MHz; diameters are 330 and 280 nm; suspended lengths are 11.8 and 5.8 μm.) **b**, Spectra of the SiNW resonator in **a** showing the peak amplitude varies linearly over nearly a decade of driving voltage (inset). **c**, Scaling of SiNW resonance frequency with geometry. The low scatter and high *Q*-values are together indicative of uniform, low-loss clamping.

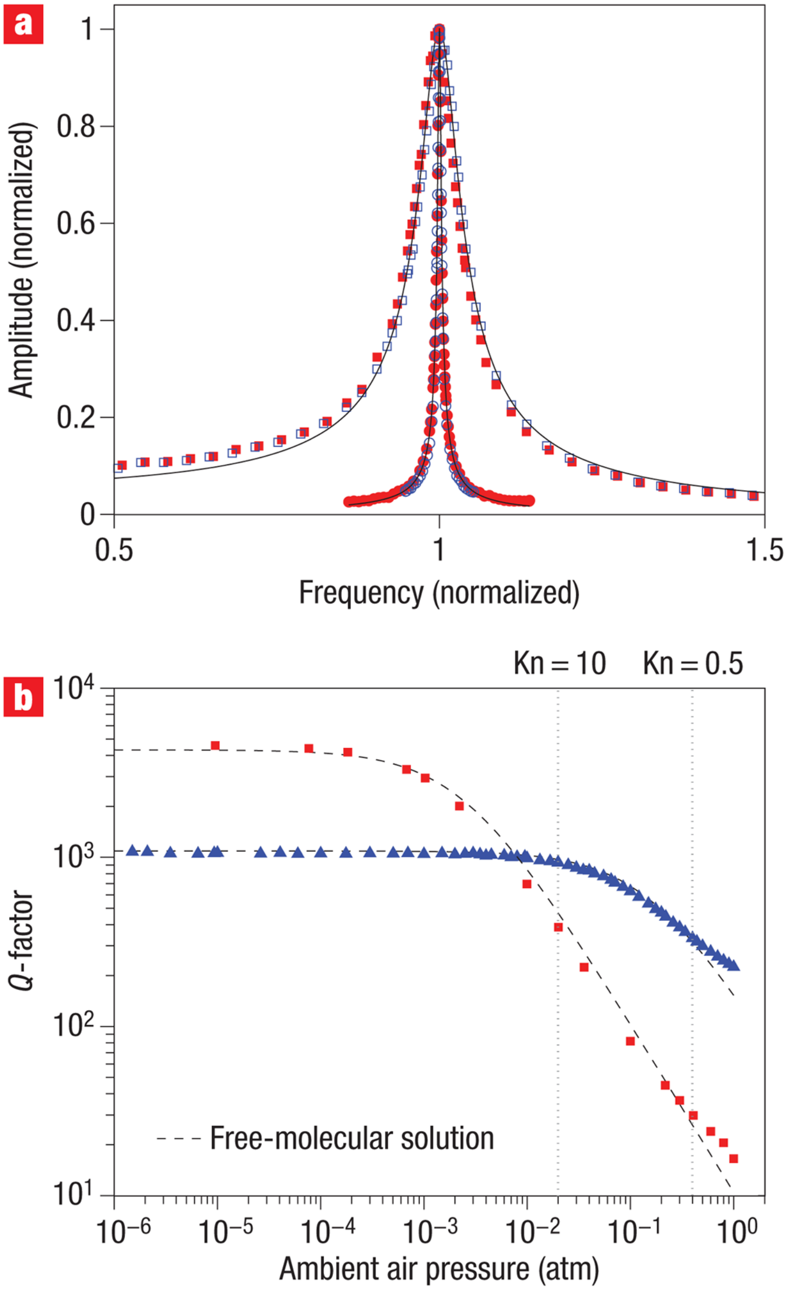

Figure 4. Pressure-dependence of NW resonator spectra

The spectra correspond to the same resonators measured in Fig. 3a and were measured in dry nitrogen. **a**, Normalized resonant spectra for Si- (outer curve) and RhNW (inner curve) at 1 atm. Forward (red squares) and reverse (blue squares) sweeps are coincident with best-fit lorentzian curves yielding *Q*-factors of 210 and 18 for Rh- and SiNW resonators. **b**, Variation of *Q*-factor with ambient pressure for the same Si- (red squares) and Rh- (blue triangles) NW resonators as in **a**. The dashed lines show the free molecular solutions for each NW resonator. The crossing in *Q*-factors for these particular Si- and RhNW resonators can be accounted for by differences in their geometry and material properties.